Arabian Journal for Science and Engineering (2024) 49:14787–14802
https://doi.org/10.1007/s13369-024-08810-3

RESEARCH ARTICLE-MECHANICAL ENGINEERING

# Investigation of Rupture Risk of Thoracic Aortic Aneurysms via Fluid–Structure Interaction and Artificial Intelligence Method

Murat Koru[1] · Gökhan Canbolat[2] · Fatih Darıcık[2] · Oguz Karahan[3] · Mustafa Etli[3] · Ergün Korkmaz[1]

Received: 27 September 2022 / Accepted: 28 January 2024 / Published online: 5 March 2024


## Abstract

Patient-specific studies on vascular flows have significantly increased for hemodynamics due to the need for different observation techniques in clinical practice. In this study, we investigate aortic aneurysms in terms of deformation, stress, and rupture risk. The effect of Ascending Aortic Diameter (AAD) was investigated in different aortic arches (19.81 mm, 42.94 mm, and 48.01 mm) via Computational Fluid Dynamics (CFD), Two-way coupling Fluid–Structure Interactions (FSI) and deep learning. The non-newtonian Carreau viscosity model was utilized with patient-specific velocity waveform. Deformations, Wall Shear Stresses (WSSs), von Mises stress, and rupture risk were presented by safety factors. Results show that the WSS distribution is distinctly higher in rigid cases than the elastic cases. Although WSS values rise with the increase in AAD, aneurysm regions indicate low WSS values in both rigid and elastic artery solutions. For the given AADs, the deformations are 2.75 mm, 6. 82 mm, and 8.48 mm and Equivalent von Mises stresses are 0.16 MPa, 0.46 MPa, and 0.53 MPa. When the rupture risk was evaluated for the arteries, the results showed that the aneurysm with AAD of 48.01 mm poses a risk up to three times more than AAD of 19.81 mm. In addition, an Artificial neural network (ANN) method was developed to predict the rupture risk with a 98.6% accurate prediction by numerical data. As a result, FSI could indicate more accurately the level of rupture risk than the rigid artery assumptions to guide the clinical assessments and deep learning methods could decrease the computational costs according to CFD and FSI.

**Keywords** Computational fluid dynamics (CFD) · Fluid–structure ınteractions (FSI) · Deep learning · Artificial neural network (ANN) · Safety factor · Vascular flow

## 1 Introduction

Computational studies on hemodynamics have increased in recent years due to the lack of clinical techniques used for cardiovascular diseases such as aneurysms, dissections, and ruptures. Ascending Thoracic Aortic Aneurysm (ATAA) is addressed by the dilation that occurs gradually over the years and could lead to dissection or rupture in the cardiovascular structure [1].

✉ Gökhan Canbolat
gokhan.canbolat@alanya.edu.tr

1 Department of Mechanical Engineering, Applied Science University of Isparta, Isparta, Turkey

2 Department of Mechanical Engineering, Alanya Alaaddin Keykubat University, Antalya, Turkey

3 Department of Cardiovascular Surgery, Alanya Alaaddin Keykubat University, Antalya, Turkey

ATAA is a life-threatening emergency in cardiovascular systems with substantial mortality. Ruptures and dissections are mainly associated with the initiation and progression of ATAA. Aortic aneurysms can be grouped under two headings, Thoracic Aortic Aneurysms (TAAs) and Abdominal Aortic Aneurysms (AAAs). This study was conducted to investigate the TAA and compare it to a normal aortic subject. The techniques of Ultrasound, Magnetic Resonance Imaging (MRI), and Computed Tomography Angiography (CTA) are used to detect an aneurysm in clinics [2]. However, the risk of dissection or rupture can not be determined only by this technique. Generally, the risk of dissection or rupture is accepted when the aneurysm diameter is bigger than 5 cm. However, rupture or dissection may occur when the aneurysm diameter is smaller than 5 cm. Therefore, numerical studies have advantages in evaluating aneurysms of patients with aortic aneurysms.

Finite Element Analyses (FEA) and Computational Fluid Dynamics (CFD) are widely used in the literature to investigate vascular flows. The various studies were performed by only CFD or FEA methods. Rigid artery models were solved by various researchers in CFD studies [3–6]. However, the deformations, von Mises stress, and rupture risk may not be investigated only by the CFD analysis because the rigid wall assumption is valid in CFD. Although the FSI analyses are computationally expensive, they have more advantages in assessing the aneurysms when they are used by accurate boundary conditions.

In the literature, some researchers used the FSI in vascular flows. Brown et al. [7] compared a cylindrical-shaped vessel and a patient-specific thoracic aorta by using FSI. They examined the physics of the flow in the two geometries to determine how they can be the most effective clinical workflow. They concluded that in the context of some clinical questions, the simpler analysis methods may capture the important characteristics of the flow field. Suito et al. [8] presented an FSI study on the blood flow and geometrical characteristics in the thoracic aorta. They focused on the relationship between the flow field and the wall shear stress distribution. They concluded that, in an area where a high WSS, the torsion contributes to decreasing the peak WSS value by expanding the high WSS region. This observation suggests that torsion has an important effect on the flow field and WSS in arteries. Gao et al. [9] present a study that considered the stress distribution in a layered aortic arch with FSI. They constructed a three-dimensional layer of aortic arc based on the aortic structure and shape. The pulsatile blood flow and artery structure were simulated utilizing coupling fluid–structure interaction analyses. They showed the variations of circumferential stress are very similar to variations in pressure. They conclude that circumferential stress in the aortic flows is directly associated with pressure, high stress on the aortic wall, and supporting the clinical importance of blood pressure control may be a risk factor for aortic dissections. Crosetto et al. [10] presented research on blood flow and arterial deformation of a normal aorta by using the FSI method. They report the result of 3D simulations on a physiological geometry over several heartbeats with different boundary conditions in the proximity of the aortic valve. They compared the FSI results with a CFD simulation with rigid wall assumption. They concluded that a difference in the WSS magnitude is overestimated in rigid walls. Campobasso et al. [11] investigated the role of the variation of peripheral resistance and the impact of aortic stiffness for peak wall stress in ATAA by using FSI. Fluid–structure interaction analyses were performed by using patient-specific aortic arches and boundary conditions, and WSSs were assessed in the ascending thoracic aorta. They conclude that a stiffer TAA may have the most altered wall stress and the change of peripheral resistance could significantly raise the risk of rupture for a stiffer aneurysm.

Artificial intelligence methods have different application areas such as medicine, robotics, image processing, the manufacturing industry, education, and computing [12]. Artificial intelligence methods include deep learning, computer vision, machine learning, and artificial neural networks. Here, the method of ANN is used frequently in artificial intelligence [13] and it works like brain neurons. ANN estimates outputs from input variables and it is first trained on training data with input variables. After training, the testing data can be predicted using the outputs of the training dataset [14]. ANN method also could reduce the computational cost and time according to theoretical, numerical, and experimental methods. It was stated in a study that CFD studies are an effective tool in terms of determining hemodynamic factors in medical applications, but it was emphasized that due to the high effort required in terms of both time and computational costs, the time and computational costs required for machine learning can be reduced and results can be obtained in shorter times. In this study, it was aimed to estimate the vessel geometry, blood density, dynamic viscosity and flow velocity parameters, and shear stress by artificial intelligence. As a result, it was stated that shear stresses at any time step in the cardiac cycle can be estimated by the coefficient of determination varied between 0.93 and 0.948 [15]. In a study, it has been stated that studies on cardiovascular studies by numerical analysis are costly in terms of computers, time, and data and it increases the interest in deep learning methods It is aimed to predict the stresses on the aorta with a deep learning model. The data obtained from the numerical analyses were determined as input for deep learning and it was stated that the stresses could be estimated with an average error of 1% with deep learning [16].

In this study, we focused on the deformation and rupture risk of the ATAA by comparing the AAD via two-way coupling FSI and deep learning. An aortic geometry obtained by a normal subject and two geometries obtained by a patient with an aneurysm scanned with an interval of a year were used in numerical studies. Aortic geometries were obtained by the CTA and the boundary conditions were applied according to the Electrocardiography (ECG) and the echocardiography (ECHO) of the patients. Rigid and elastic artery flow models were solved by the non-Newtonian Carreau model with a UDF code that represents the patient-specific velocity waveform obtained by the Echocardiography (ECHO). Deformations, wall shear stress (WSS), von Mises stress, and rupture risk according to safety factors addressed by the ultimate tensile strength of the aorta were presented in this study. The rigid and elastic artery assumptions were compared to assess the difference in WSS for aortic geometries by transient simulations. The results showed that FSI analyses are needed to evaluate the rupture risk because the rigid artery assumption (CFD) overestimates the WSS and the study shows that only WSS values could not efficiently assess aortic rupture. In addition to CFD and FSI analyses, deep learning could be used to decrease computational cost and time. Because transient numerical simulations were about 30 h for CFD and it was 120 h per geometry during the cardiac cycle. In this study, a preliminary work on deep learning was presented by three aortic geometries in terms of rupture risk addressed by safety factors and it could be expanded by many CFD and FSI calculations for individuals. We conclude that the rupture risk evaluated by the safety factors of the arteries can guide clinical assessments and predictions.

## 2 Methodology

Generation of 3-D models of aortic arches from CTA, segmentation process, generation of mesh, and mesh independency test are presented in this section. We presented here boundary conditions and governing equations with the numerical approaches.

### 2.1 Segmentation, Generation of 3D Models and Aortic Meshes

In this study, three tomographies with different ascending aortic diameters were used in the rigid artery and elastic artery analyses. One of them was obtained from a normal subject and two of them were obtained from a subject with an aortic aneurysm. During the generation of 3D model of the aortic arches, the ascending aortic, descending aorta, and three main branches of the aorta were segmented to perform numerical simulations. They were obtained by 3D CTA which is a 16-slice multi-system (16 Multi-Slice, Alexion, Toshiba, and Japan). Figure 1 shows the segmentation process from 3D CTA to 3D model. As seen in the figure, an inlet and four outlets on the aorta are defined as inlet and outlet boundary conditions. If we consider this as a control volume, the flow rates entering and leaving the aorta are equal. With the opening of the aortic valve, blood begins to be pumped into the aorta and it is distributed throughout the body by the three branches of the aorta and the descending aorta. Since this study studied thoracic aortic aneurysm, the aortic model was preserved only with the thoracic aortic side.

After the segmentation process, aortic geometries were prepared to generate the meshes. The solid models of aortic arches and three main branches of the aorta were generated by using 3-Matic Medical software. Solid and fluid domains were created at this stage.

Figure 2 shows the 3D models of aortic arches used in this study. Ascending aorta models with different ascending aortic diameters were presented and meshed for numerical calculations. Figure 3 shows the meshed views of aortic arches.

Three different models were meshed with the mesh independency tests by the Fluent meshing tool. Aortic arches have complex topologies. Therefore, all triangular elements were used for volume and solid domains to obtain uniform mesh.

Mesh independency tests are a vital part of numerical simulations to obtain sufficient mesh element numbers. Therefore, mesh independence tests were performed to reduce computational cost depending on the area-weighted average WSS of the wall. Mesh element size was decreased gradually and sufficient element numbers were used to perform numerical calculations. Approximately 1.2 million, 1.05 million, and 1.25 million tetrahedral elements were used for the aortic branches with 19.81 mm, 42.94 mm, and 48.01 mm ascending aortic diameters, respectively. Skewness values were kept under 0.5 during the meshing process. During the generation of meshes, 12 layers of inflation and a 1.2 growth rate were utilized to predict flow characteristics in the boundary layer.

### 2.2 Boundary Conditions, Governing Equations, and Numerical Methods

The blood was assumed as homogeneous, and incompressible. The flow is assumed laminar and fully developed in this study. The density of the blood is 1060 kg/m$^3$ and the non-Newtonian blood assumption was considered in this study. The wall of the artery was considered as both rigid and linear elastic in numerical studies. Rigid and elastic artery models were also compared to investigate the differences. A no-slip boundary condition was applied to the artery. We implemented 120 mmHg for outlets in arteries as an outflow boundary condition according to the ECG and ECHO data of the subjects. Three main branches of the aorta are extended for fully developed flow in outlets.

In this study, a patient-specific velocity waveform was used to reflect the real pulsatile flow in the aorta as in our previous study [17] in Fig. 4. The velocity waveform was obtained according to the ECHO of the subject. The real-patient pulsatile flow was provided with a User Defined Function (UDF) code in the commercial software of ANSYS-Fluent by the version of 2019 R3. This UDF code was generated considering the phases of the Isovolumic Contraction Phase (ICP), Ejection, and the Isovolumic Relaxation Phase (IRP) in the cardiac cycle. The systolic phase starts with the ICP and ends with the IRP.

The linear elastic assumption was used in this study and it was used in many kinds of research performed by the FSI [8, 10, 18, 19]. In this study, the mechanical properties of the arteries were used as follows; the aortic thickness ($t$) is 2 mm [9, 20], Young modulus ($E$) is 1 MPa [21, 22], ultimate

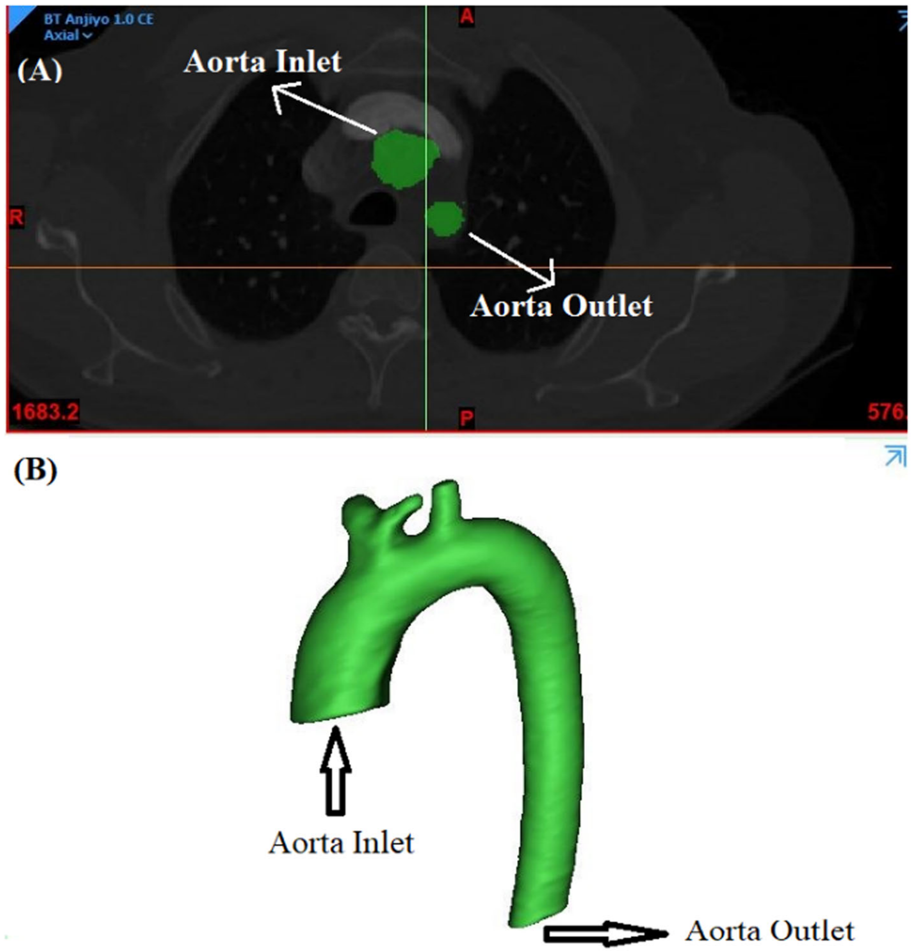


**Fig. 1** Segmentation process of aortic arch by using commercial software of Mimics **a** 3D-CTA axial view, **b** generated 3D model of the aortic arch

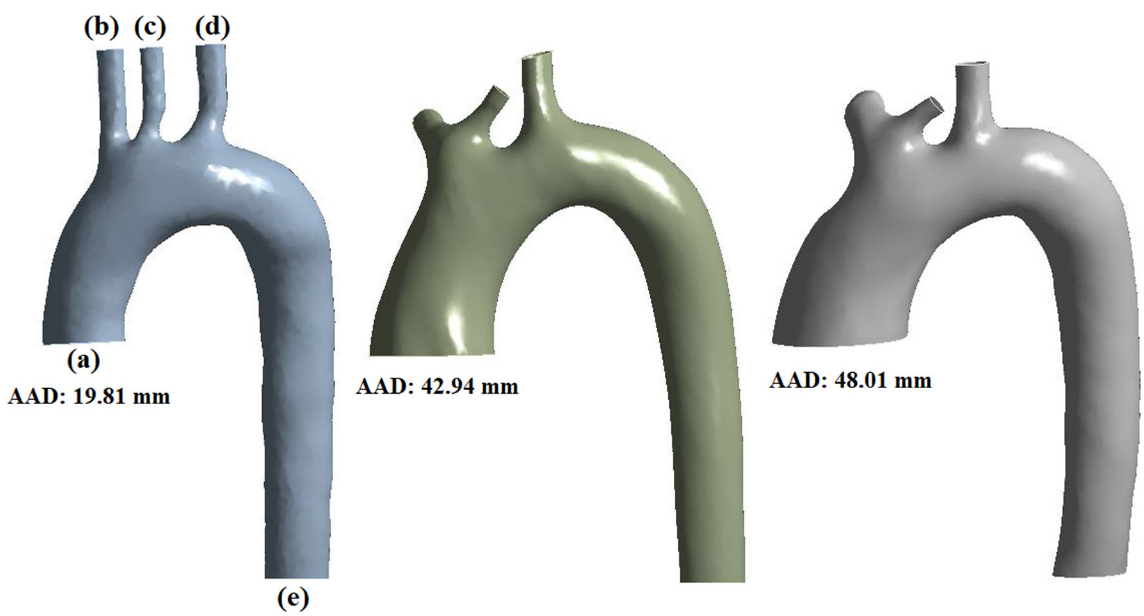


**Fig. 2** Three segmented aortic arches with different AADs (19.81 mm, 42.94 mm, and 48.01 mm) **a** inlet of ascending aorta, **b** brachiocephalic artery, **c** common carotid artery, **d** left subclavian artery, and **e** outlet of descending aorta

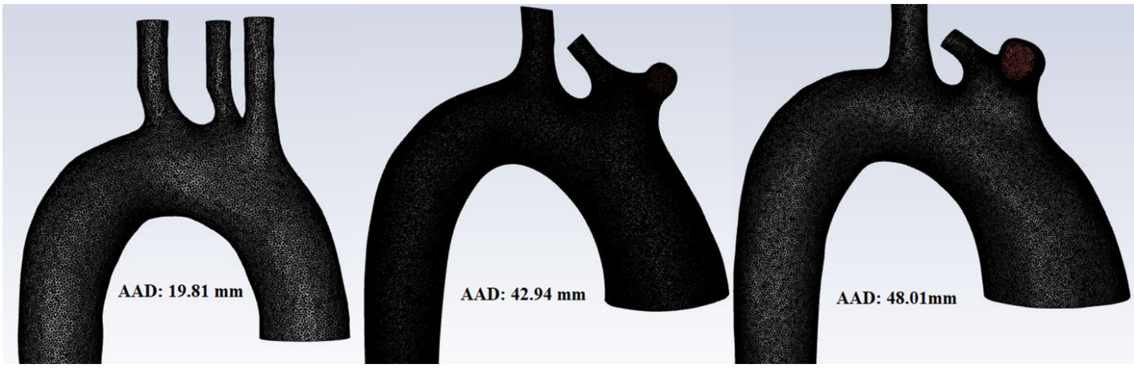


**Fig. 3** Generated meshes for the three aortic arches with different AADs

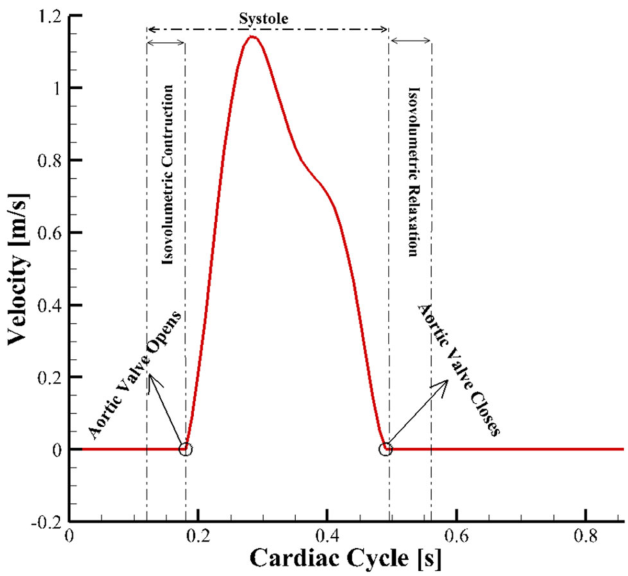


**Fig. 4** The patient-specific velocity waveform obtained by ECHO

tensile strength ($\sigma_{ut}$) is 1.25 MPa [23], Poisson ratio ($\nu$) is 0.45, and density of the artery ($\rho$) is 1120 kg/m$^3$ [24, 25].

Although the nature of blood flow is non-Newtonian in arteries, various researchers have used the Newtonian blood assumption in FSI studies [7, 18, 22, 25–31]. However, this study presents a non-Newtonian blood flow. The governing equation (Eq. 1) is given below for the Carreau viscosity model [32],

$$\mu = \mu_\infty + (\mu_0 - \mu_\infty)1 + \left(\lambda\dot{\Upsilon}\right)^{2\frac{n-1}{2}} \tag{1}$$

where $\lambda = 3.313$ is relaxation time (s), n = 0.3568 is the power index, $\mu_0 = 0.056$ viscosity at zero shear rate (Pa s), $\mu_\infty = 0.00345$ viscosity at the infinite shear rate (Pa s), and shear rate $\dot{\Upsilon}$ [s$^{-1}$] [33].

In this study, we used the two-way coupling FSI method with the Arbitrary Lagrangian–Eulerian (ALE) approach. It was used to integrate fluid mechanics and solid mechanics for a coupled solution. The equation of Cauchy's law for the motion is derived to balance the forces. The product of the velocity and density is balanced with the divergence of the stress tensor and other body forces.

$$\rho_f\left[\frac{\partial \mathrm{u}}{\partial \mathrm{t}} + \mathbf{u}\cdot\nabla\mathbf{u}\right] = \nabla\cdot\sigma + \mathrm{f} \tag{2}$$

where $\rho$ is density density, $\mathbf{u}$ is the velocity vector, $\sigma$ is the Cauchy stress tensor, and f is the external body force. f is neglected due to the lack of external forces. The displacement of the fluid–solid interface and fluid domain is derived from the ALE configuration [25, 34].

The governing equations of fluid domain;

$$\rho_f\left[\frac{\partial u_f}{\partial t} + u_f\cdot\nabla u_f\right] = -\nabla p + \mu\nabla^2 u_f \tag{3}$$

$$\nabla\cdot u_f = 0 \tag{4}$$

where $\rho_f$ is the density, $u_f$ is the velocity vector, $\mu$ is the dynamic viscosity, and $p$ is the pressure in the fluid domain.

The governing equations of solid domain;

$$\rho_s\frac{\partial^2 d_s}{dt^2} = \nabla\cdot\sigma_s \tag{5}$$

where $d_s$ is the solid displacement, $\rho_s$ is the density of the solid domain, $\sigma_s$ is the Cauchy stress in the solid domain. The forces and velocities must be equal in the fluid–structure interface.

$$u_f = u_s \tag{6}$$

and

$$\sigma_s\cdot n = \Gamma\cdot n \tag{7}$$

where $n$ is the normal vector, $\sigma_s$ is the Cauchy stress, and $\Gamma$ is the real stress.

The outlets of the arteries were fixed and the inner side of the arteries was specified as a fluid–solid interface. FSI coupling is to transfer loads calculated with a fluid solver into the structural domain and displacement of the structure is also transferred to the fluid solver [35]. The solution was performed by the coupled pressure–velocity method in time-dependent solutions. The second-order upwind spatial discretization was used to discretize the momentum, velocity, and pressure. The convergence criteria are $10^{-4}$ for residuals in fluid flow. The time step size is $10^{-4}$ and 3080-time steps were calculated to represent the systolic phase of the cardiac cycle. Remeshing was used in dynamic mesh for all time steps. System coupling was used to couple Fluent and Transient Structural in ANSYS. Solutions were performed by an Intel Xeon 2 X 4214R 12C computer with 64 GB of RAM.

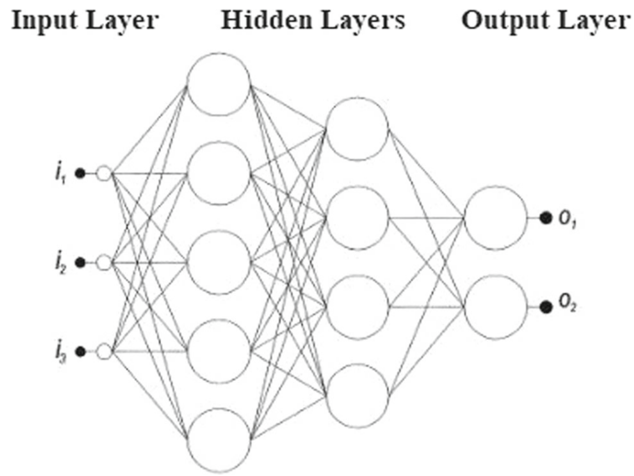


**Fig. 5** ANN algorithm [37]

### 2.3 Construction of Artificial Neural Networks

Deep learning is a set of algorithms called ANNs inspired by the structure and function of the brain, as well as a subbranch of machine learning. Deep learning is a machine learning technique that teaches computers about situations that humans may encounter, such as nature. Deep learning is the basic idea behind autonomous vehicles and is a technique that teaches vehicles about traffic signs, pedestrians, and any obstacle. In deep learning, computational models consisting of multiple processing layers allow the learning of multiple representative data. Deep learning explores complexity in large datasets by using the backpropagation algorithm to specify how a machine should change the parameters used to calculate the representation in each layer from the data in the previous layer [36].

In this study, the neural network algorithm is used to predict the rupture state of the vessels. ANN consists of artificial neurons and these artificial neurons are copies of human brain neurons. Neurons in the brain transmit signals to perform actions, and these neurons are connected to a neural network to perform tasks.

A neural network model consists of three layers as seen in Fig. 5. It contains input neurons that send information to the hidden layers, the first layer is the input layer. The hidden layer performs calculations on the input data and transfers the result to the output layer. In addition, while $i_1$, $i_2$, and $i_3$ in the figure represent the input vectors, $O_1$ and $O_2$ represent the output vectors. The deep learning model is developed in Python language using the Jupyter Notebook interface via Anaconda software. Pandas, Numpy, Seaborn, Matplotlib.pyplot, Sklearn, Tensorflow, and Keras libraries were used during the study. In the study, the data in 648 time steps were taken from the numerical data carried out based on transient simulations of individuals. During the construction of deep learning, time, viscosity, density, ascending aortic diameters, shear stress values, deformations, and von Mises stresses were determined as variables, that is, the input layer and the safety factor indicating the rupture risk in the arteries was determined as the output layer.

The data set is divided into 80% training and 20% test data. The sequential model is used as the model from the Keras library, which creates a linear stack of layers. The dense layer model has also been used to create regular and deep neural networks. Relu for the activation function and Rmsprop for the optimizer were used in the ANN model. Mean Square Error (MSE) was used for the loss function and it is frequently used in regression. Loss (L) is average data where the differences between the actual and predicted. The MSE was used for the loss function shown in Eq. (8). Coefficient of determination ($R^2$) was used as performance measurement criteria in Eq. (9).

$$\mathrm{L} = (\mathrm{y}, \widehat{\boldsymbol{y}}) = \frac{1}{N}\sum_{i=0}^{N}(\mathrm{y} - \widehat{\boldsymbol{y}})^2 \tag{8}$$

$$\mathrm{R}^2 = 1 - \frac{\sum_{t=1}^{n}\left(y_t - y_{pre}\right)^2}{\sum_{t=1}^{n}\left(y_t - y_{avg}\right)^2} \tag{9}$$

In the equations, $y_t$ represents the numerical data. $y_{est}$ represents the estimated values, and the $y_{avg}$ represents the average values [38]. The deep learning dataset is given in Table 1. In the dataset nine input variables (Cardiac interval, velocity, density, AAD, WSS, deformation, and stress) and an output (Safety factor) are seen for the ANN algorithm. In the ANN, the number of hidden layers, number of neurons, batch size, and epoch size are important parameters. To obtain the highest $R^2$ performance for the ANN model, three hidden

**Table 1** Deep learning dataset

| Data | Cardiac Interval | Velocity | Viscosity | Density | AAD | WSS | Pressure | Deformation | Stress | Safety Factor |
|---|---|---|---|---|---|---|---|---|---|---|
| 1 | 0 | 0.001 | 0.0035 .6635 | 1060 | 19.81 | 0 | 16,000 | 0 | 0 | 182 |
| 2 | 0.004 | 0.001 | 0.0035 0.0035 | 1060 | 19.81 | 0.0002 | 16,000 | 0.001616 | 0.0001 | 182 |
| 3 | 0.008 | 0.001 | 0.0035 | 1060 | 19.81 | 0.0001 | 16,000 | 0.00103 | 0.0001 | 182 |
| 4 | 0.0012 | 0.001 | 0.0035 | 1060 | 19.81 | 0.0001 | 16,000 | 0.00084 | 0.0001 | 182 |
| … | ••• | ••• | ••• | ••• | ••• | ••• | ••• | ••• | ••• | ••• |
| … | ••• | ••• | ••• | ••• | ••• | ••• | ••• | ••• | ••• | ••• |
| … | ••• | ••• | ••• | ••• | ••• | ••• | ••• | ••• | ••• | ••• |
| 285 | 0.268 | 1.105 | 0.0035 | 1060 | 42.94 | 25.613 | 18,970.52 | 6.435 | 0.434 | 2.775 |
| 265 | 0.2272 | 1.123 | 0.0035 | 1060 | 42.94 | 26.24 | 18,846.78 | 6.593 | 0.444 | 2.709 |
| 287 | 0.2276 | 1.136 | 0.0035 | 1060 | 42.94 | 26.707 | 18,705.14 | 6.71 | 0.452 | 2.661 |
| … | ••• | ••• | ••• | ••• | ••• | ••• | ••• | ••• | ••• | ••• |
| … | ••• | ••• | ••• | ••• | ••• | ••• | ••• | ••• | ••• | ••• |
| … | ••• | ••• | ••• | ••• | ••• | ••• | ••• | ••• | ••• | ••• |
| 645 | 0.848 | 0.001 | 0.0035 | 1060 | 48.01 | 0.8733 | 15,975 | 0.06393 | 0.0115 | 41 |
| 646 | 0.852 | 0.001 | 0.0035 | 1060 | 48.01 | 0.8601 | 15,975 | 0.06303 | 0.0113 | 41 |
| 647 | 0.856 | 0.001 | 0.0035 | 1060 | 48.01 | 0.8472 | 15,976 | 0.06216 | 0.0111 | 41 |
| 648 | 0.86 | 0.001 | 0.0035 | 1060 | 48.01 | 0.8346 | 15,976 | 0.0613 | 0.011 | 41 |

layers with 16 neurons, 10 batch size, and 1000 for epoch size were determined.

## 3 Results

Figure 6 presents the wall shear stress distribution of the three different aortic arches for the peak systolic phase. The left column shows the rigid artery assumptions and the right column shows the elastic artery assumption. In this study, rigid and elastic artery assumptions were compared using numerical analyses.

The peak systole is the most important and informative phase in the cardiac cycle.

in terms of cardiovascular risk factors [39, 40]. Therefore, the WSS distribution of three thoracic aortic arches was presented in this phase. The comparison of the rigid and elastic arteries is seen in Fig. 6. It is obvious in Fig. 6 that the WSS distribution in rigid artery solutions is higher than in elastic artery solutions. The case of AAD of 19.81 mm presents a similar WSS distribution for both rigid and elastic arteries. While the WSS stress is nearly 13 Pa along the wall, it is almost 30 Pa in the vicinity of bifurcation due to the nature of the flow in this area. The expansion of the elastic arteries caused a decrease in the velocity in the elastic arteries and therefore a decrease in the WSS. Similarly, expansion of the elastic artery in the aneurysms showed lower WSS distributions. The decrease in WSS in the elastic state of the healthy individual compared to the rigid state is considerably lower than in the elastic cases with 42.94 mm AAD and 48.01 mm AAD. This situation may result from the elastic deformation difference of the models, in which a more uniform deformation occurred at the aorta of a healthy individual.

Figure 7 shows the area-weighted average WSS variations along the arteries during the systolic phase. While red lines represent the elastic wall assumption, green lines represent the rigid wall assumption. The rigid artery solutions indicate a higher area-weighted average WSS than the elastic artery solutions. The area-weighted average WSS difference between the rigid and elastic artery assumptions is 15.5% during the systolic phase for 19.81 mm AAD. It is 20.5% and 22% for the 42.94 mm and 48.01 mm AADs, respectively. The variation of area-weighted average WSS shows also the higher WSS in rigid artery assumptions.

Figure 8 shows the distribution of total deformation in aortic arches and Fig. 9 shows the equivalent von Mises stress along the artery at the peak systolic phase.

The total deformation in AAD of 19.81 mm is 2.75 mm, while it is 6.82 mm and 8.48 mm for the AADs of 42.94 mm and 48.01 mm, respectively. It is shown in Fig. 8 that the increase in AAD increased the deformation in the aneurysm cases. At 42.94 mm AAD, the deformation is more than two

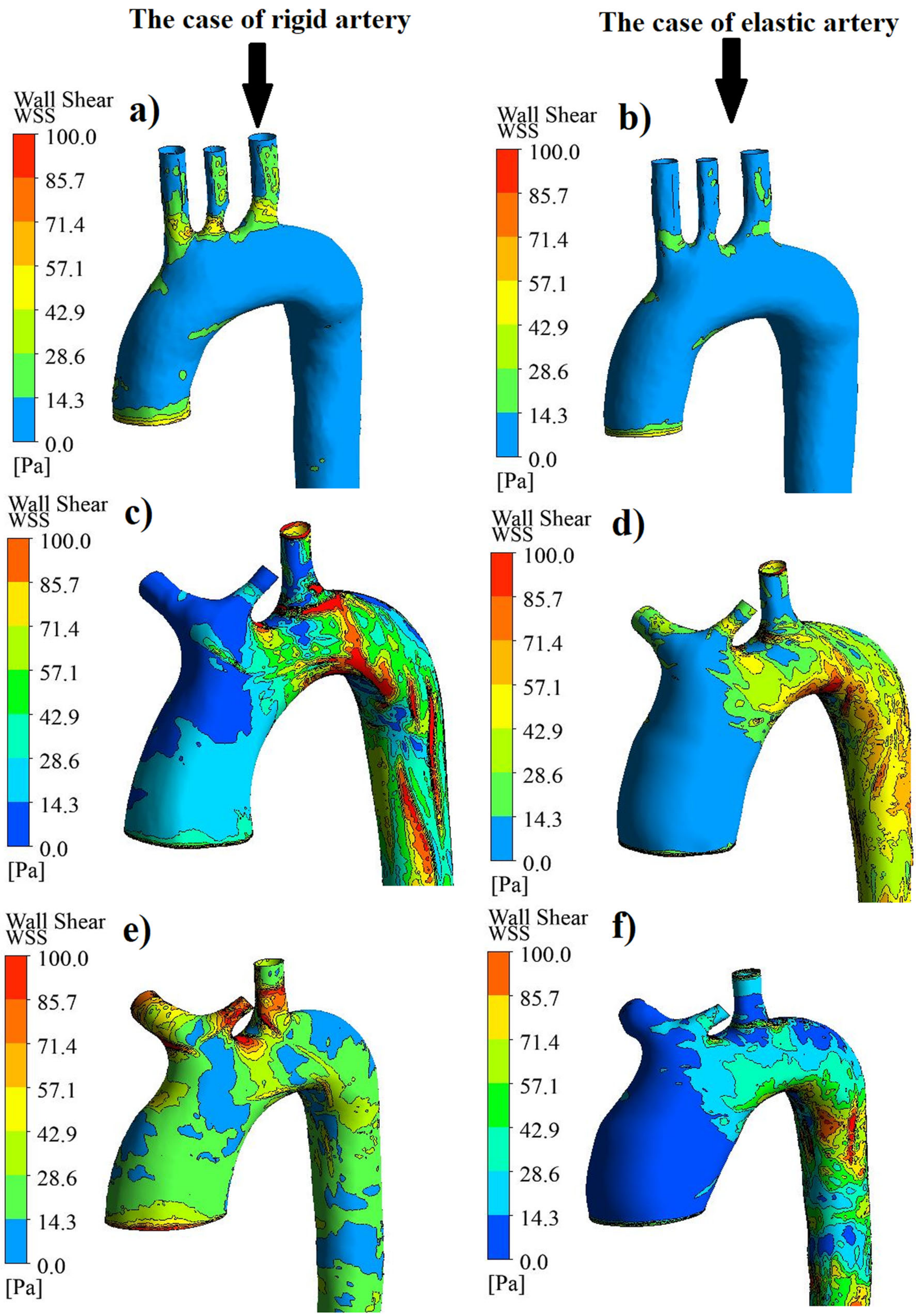


**Fig. 6** WSS distributions, **a** the rigid case in AAD of 19.81 mm, **b** the elastic case in AAD of 19.81 mm, **c** the rigid case in AAD of 42.94 mm, **d** the elastic case in AAD of 42.94 mm, **e** the rigid case in AAD of 48.01 mm, and **f** the elastic case in AAD of 48.01 mm

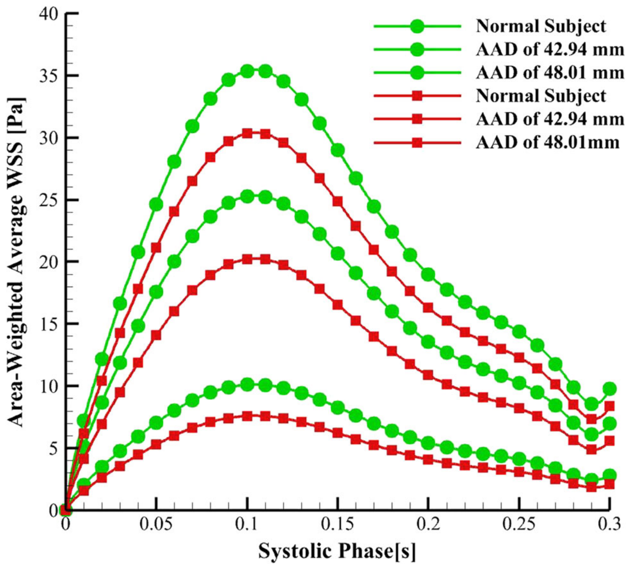


**Fig. 7** The variation of WSS along the artery during the systolic phase for the rigid and elastic artery assumptions

times that of a normal person, and at 48.01 mm AAD, the deformation is more than three times that of a normal subject.

On the other hand, Fig. 9 shows that maximum equivalent von Mises stresses are 0.16 MPa, 0.46 MPa, and 0.53 Mpa in ascending aorta for 19.81 mm, 42.94 mm, and 48.0 mm AADs respectively. von Mises stress is over two times in 42.94 mm AAD and it is over three times in 48.01 mm AAD according to the normal subject. The increase in equivalent von Mises resulted in a rise in deformations, as expected.

The increase in AAD changes the flow structure and the pressure load in the aneurysm region. As the pressure load on the artery wall increases, deformations and stress gradually increase. In cases with aneurysms, the increase in AAD is 11%, the increase in maximum deformation is 24%, and the increase in maximum stress is 15%. These results show that the increase in deformation and stress is not proportional to the increase in ADD.

Moreover, there are differences between changes in stress and changes in deformation. Since we assumed that the tissue of the aorta would exhibit linear elastic behavior, the change in deformation is also related to the topology of the tissue. Therefore, we can mention the influence of the aneurysm on the excessive deformation at peak systole. Besides all these findings, aneurysmal tissues have lower elasticity than healthy tissues, unlike our assumptions. Lower elasticity causes restricted deformation and increased stress. These results are consistent with the known loss of elastic fibers in aortic aneurysm [41] and TAA formation causes loss of elastic fibers and structural integrity [42].

Figure 10 shows the safety factor distribution along the artery walls for the three different cases of AADs. In Fig. 10, AAD increases downwards with 19.81 mm, 42.94 mm, and 48.01 mm, respectively. The safety factor is between 10 and 15 for the 19.81 mm AAD with the blue color along the artery. However, it decreases to 2.62 and 2.15 for the 42.94 mm and 48.01 mm AADs, respectively. An increase in ascending aortic diameter decreases the safety factor due to a loss in elasticity.

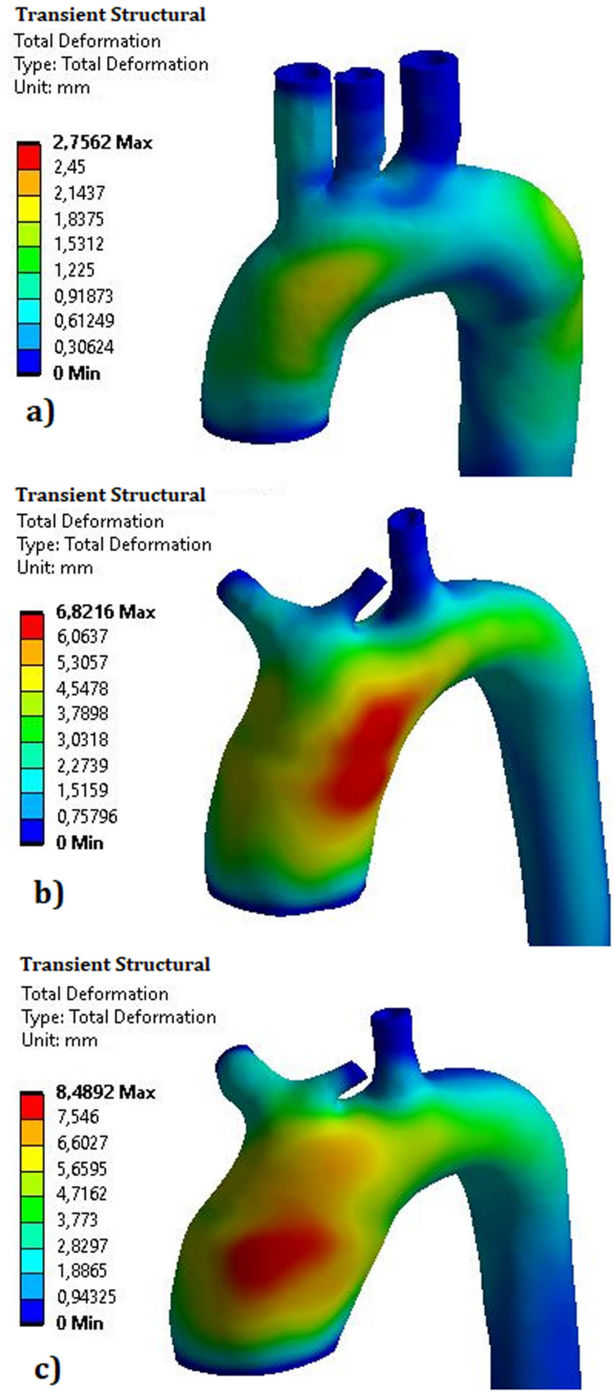


**Fig. 8** Deformation distributions along the aortic arches **a** 19.81 mm AAD, **b** 42.94 mm AAD, and **c** 48.01 mm AAD

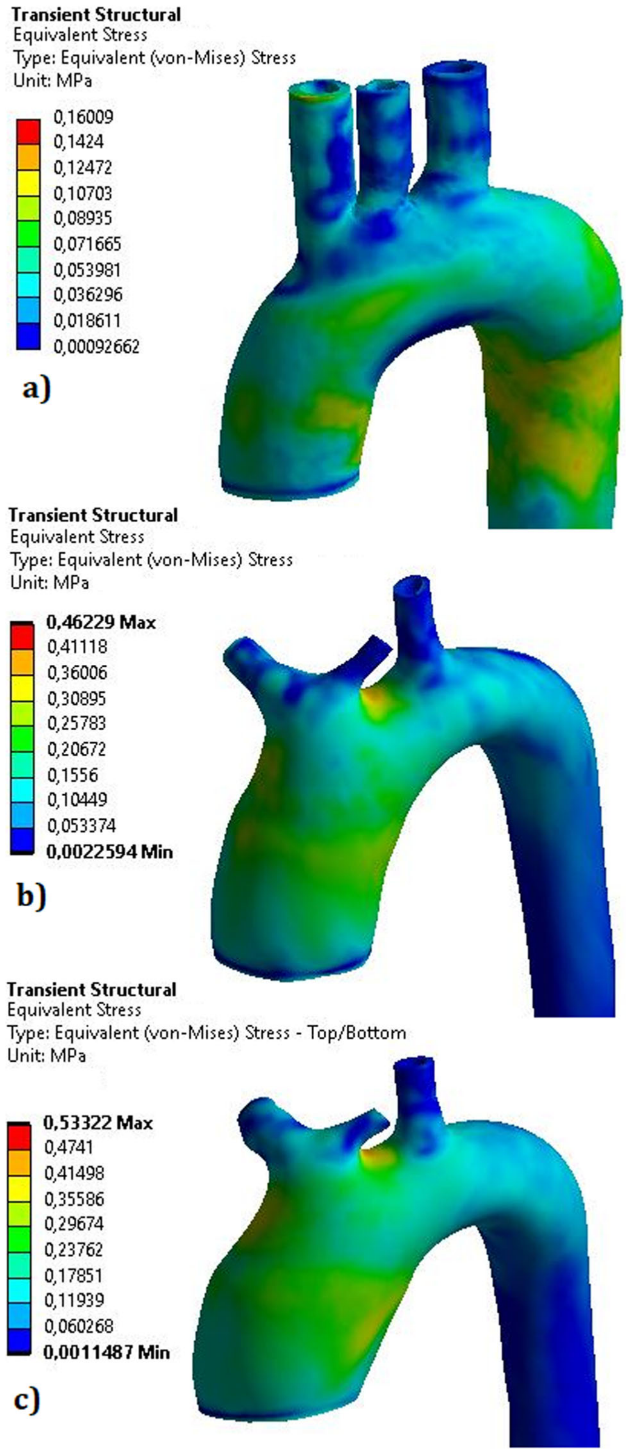


**Fig. 9** Equivalent von Mises stress distributions along the aortic arches **a** 19.81 mm AAD, **b** 42.94 mm AAD, and **c** 48.01 mm

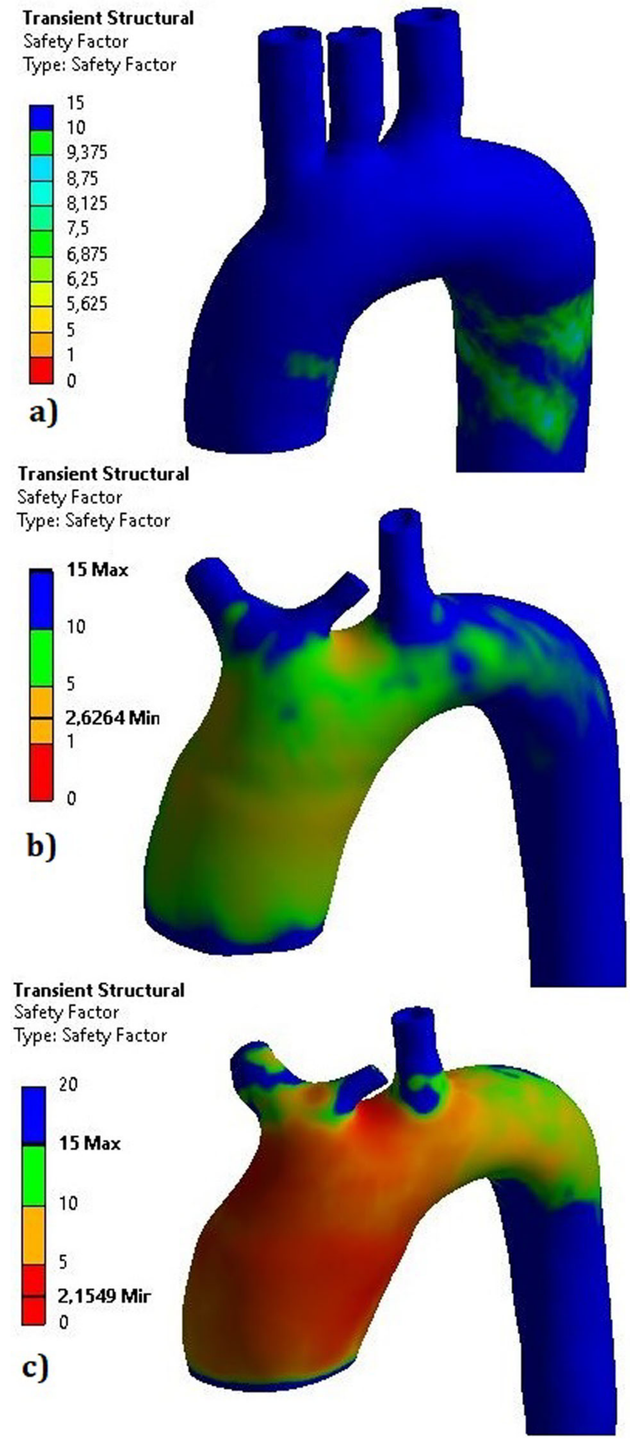


**Fig. 10** Safety factor distributions along the aortic arches **a** 19.81 mm AAD, **b** 42.94 mm AAD, and **c** 48.01 mm

The safety factor is defined as the ratio of the strength of the structure to the applied maximum stress in the body and it is given below. The allowable value is 1. A value below 1 results in the failure.

For the 19.81 mm AAD, the safety factor is higher than 10, as expected in terms of rupture risk under normal circumstances. Because the stress that occurs along the wall is highly low according to the strength of the artery. Therefore, with the boundary conditions applied in this study, it can be said that the 19.81 mm AAD does not pose a risk potential under normal conditions. The minimum safety factor is 2.62 for the 42.94 mm AAD in some aneurysms regions but it is between 5 and 10 in the thoracic aorta predominantly in Fig. 10. Therefore it can be indicated that the AAD of 42.94 mm does not pose a potential risk according to AAD of 48.01 mm. Since the stress and pressure load increases with the decrease in the safety factor. It is shown in Fig. 10 that the safety factor decreased distinctly in the thoracic aortic region with an increase in AAD. The minimum safety factor is 2.15 along the thoracic aneurysm region for the 48.01 AAD. As a result, it appears that the 48.01 mm AAD poses a potential risk in terms of rupture under this situation and the boundary conditions applied in this study.

In the study, the results of FSI analysis in which fluid and structure interactions were utilized for the ANN model. The predictions of deep learning algorithms through the artificial neural networks were performed by the numerical results to predict rupture risk of aortic aneurysms which is the main purpose of the study. With two-way coupling FSI data, the blood ejection phases in the cardiac cycle were reflected in deep learning. Thus, the changing hemodynamic factors of the vascular flow were also taken into account in the training of the artificial neural networks model. Therefore, the cardiac cycle has taken its place as an important parameter in the training of artificial neural networks as a parameter. Figure 11 presents the ANN algorithm used in this study. It is shown that 9 neurons for input variables, 16 neurons for each of 3 hidden layers, and a neuron for the output layer are constructed for the ANN algorithm. Figure 12 shows the variation of test and prediction data for the safety factor obtained by the ANN. Here, it is shown that a near-linear variation in prediction data with test data is due to $R^2$ performance in 0.986 test and prediction data. After obtaining the most accurate algorithm by ANN, some predictions were performed according to input variables to estimate output variables as safety factors.

It is seen in Table 2 that the safety factor could be estimated according to variables of the individuals such as AAD, cardiac time, the velocity in the cardiac cycle, or density of the blood. Here, the estimations were performed according to random input variables. The advantage of deep learning is seen here. Because the estimation of the safety factor is possible in a short time within the developed algorithm instead of analyzing with large computational costs and time.

## 4 Discussion

In this study, we investigated the increase in ascending aortic diameter by using a normal aortic arch and two different aortic ascending aneurysm geometries. The progress in aneurysms was analyzed by coupled mechanics of two-way coupling FSI. The potential risk of the rupture was researched in terms of an increase in the AAD. Rigid and elastic artery assumptions were compared to determine the efficient method. It is shown that FSI solutions have more advantages in observing the deformation, stress, and rupture risk in vascular flow studies.

The mechanical properties of the artery, flow conditions, blood viscosity model, boundary conditions, and numerical methods are highly important while performing both CFD and FSI analyses. In the literature, various solution techniques with various blood properties and arterial properties have been reported in numerical analysis. In this study, patient-specific aortic domains (Fig. 2) and patient-specific boundary conditions (Fig. 4) were used to reflect the results as close as possible to actual conditions. However, it is very difficult to provide the same conditions in vascular flows.

The non-Newtonian blood viscosity was also considered in this study because the nature of the blood flow is non-Newtonian in arteries. The blood was considered Newtonian in various studies in the literature because the blood acts as Newtonian in large arteries. However, the Carreau viscosity model was used in this study since the Newtonian model underestimated the WSS. Moreover, its derivatives were used in various studies [1, 11, 26, 43–45].

The investigation of WSS is the first step generally in numerical studies on vascular flows because WSS is an important indicator of risk in rupture and dilatation, and it was stated in various studies [21, 46–49]. However, the investigation of WSS alone does not evaluate the rupture risk alone in the rigid artery assumption. It could indicate the regions with high or low shear stress but it changes in elastic artery solution. Therefore, rigid and elastic artery assumptions were presented to show differences in WSS in this study. The percent differences of 15.5%, 20.5%, and 22% were observed between the rigid and elastic artery assumptions in the peak systolic phase for the AAD cases of 19.81 mm, 42.94 mm, and 48.01 mm, respectively. The investigation of aortic flows by only rigid artery assumption could indicate WSS values more than should be, as stated in many studies. In a study [27], similar differences were observed in WSS values based on the finite element and computational fluid dynamics methods. In

**Table 2** Deep learning estimation

| Cardiac ınterval | Velocity | Viscosity | Density | AAD | WSS | Pressure | Deformation | Stress | Safety factor |
|---|---|---|---|---|---|---|---|---|---|
| 0.12 | 0.3 | 0.0032 | 1050 | 21.8 | 12.3 | 16,570 | 5.8 | 0.35 | 4.92 |
| 0.18 | 0.6 | 0.0030 | 1065 | 35.3 | 8.5 | 18,350 | 8.3 | 0.5 | 4.19 |
| 0.25 | 0.78 | 0.0035 | 1060 | 32.3 | 15.3 | 17,200 | 10.5 | 0.45 | 2.64 |
| 0.5 | 1.1 | 0.0033 | 1070 | 42.5 | 14.5 | 18,700 | 12.3 | 0.75 | 2.47 |
| 0.4 | 0.95 | 0.0031 | 1055 | 39.4 | 11.5 | 15,700 | 9.5 | 0.42 | 2.89 |
| 0.7 | 0.82 | 0.004 | 1040 | 47.5 | 16.5 | 17,900 | 11.3 | 0.55 | 2.35 |
| 0.48 | 0.35 | 0.0034 | 1080 | 43.5 | 8.5 | 16,350 | 6.2 | 0.38 | 6.39 |
| 0.32 | 0.98 | 0.0028 | 1035 | 52 | 18.5 | 17,450 | 8.9 | 0.52 | 2.33 |
| 0.21 | 0.73 | 0.003 | 1052 | 45 | 13.5 | 16,400 | 7.5 | 0.38 | 2.88 |
| 0.288 | 1.1 | 0.0035 | 1060 | 46 | 7 | 16,000 | 9 | 0.53 | 3.11 |
| 0.3 | 1.2 | 0.004 | 1070 | 55 | 20 | 17,600 | 13 | 0.8 | 1.94 |

a study [10], it is indicated that rigid wall assumption overestimated the WSS in the walls performed on aortic flow. In a study [50], both rigid and FSI simulations were performed to assess WSS, and enormous differences were found between the rigid and FSI simulations. They concluded that it is important to consider WSS in FSI simulation. In a study [51], both rigid and FSI simulations were performed, and they stated that simulation with a rigid wall assumption of the same aortic geometry overestimates the WSS concerning the FSI. In a study [52], an FSI study was performed to analyze WSS, and it was compared to the rigid artery. They also concluded that the analyses performed by rigid artery assumption overestimate the WSS according to FSI analyses, as in our study. We also presented the area-weighted average WSS in Fig. 7. It is shown that the area-weighted average WSS is higher in rigid cases than the elastic cases in all time steps in the systolic phase.

This study presents the variation of deformations according to change in AADs in Fig. 8. Total maximum deformations are 2.75 mm, 6.82 mm, and 8.48 mm for the AAD cases of 19.81 mm, 42.94 mm, and 48.01 mm, respectively. The increase in AAD was accompanied by an increase in deformations and stress. One of the main purposes is to investigate the deformation, stress, and safety factors under the same boundary conditions to compare with each other. In this way, it is shown that deformation is more than two times in the case of 42.94 mm AAD according to the normal subject and it is more than three times in the case of 48.01 mm AAD according to the normal subject. These results also indicate that the ratios of deformation to AAD are 13.8%, 15.8%, and 17.6% in the 19.81 mm, 42.94 mm, and 48.01 mm AADs, respectively. As a result, the ratio of deformation to AAD increases with the level of the aneurysm with the pressure load on the wall.

The rupture risk is evaluated by the safety factor in this study according to the ultimate tensile strength of the artery [23] in Fig. 10. In this study, we present a new perspective on the factor of safety based on the ultimate tensile strength to observe the risk of rupture by combining fluid mechanics and solid mechanics. Safety factor results presented that while it is almost 15 for the 19.81 AAD, it is approximately 5 and 2 in the cases of 42,94 mm and 48.01 mm AADs respectively in the same boundary conditions. Thus, it is obvious that the 48.01 mm AAD is 7 times more at rupture risk than the normal subject, and the 42.94 mm AAD is 3 times more at rupture risk than the normal subject. However, hypertension is one of the risk factors for rupture in aneurysms [34]. It also plays an important role in the progression and formation of aneurysms [53, 54]. Therefore, the progression of hypertension could decrease the safety factors given in Fig. 10. and it is needed to take into account that the rupture may occur in the hypertension conditions. Moreover, the decrease in safety factor can be associated with an increase in dissection or rupture risk. Although an increase in aortic diameter is associated with these risks, these numerical simulations can provide risk stratification and also identify the area most likely at risk for rupture and dissection. Additionally, the tomographical evaluation of these dynamic calculations can provide the risk classification of sudden aortic complications.

On the other hand, the deep learning side of the study provides valuable contributions to the literature. Transient numerical results were used to construct a dataset and an ANN algorithm and these results were obtained from different time steps from the cardiac cycle. At this stage, it is possible to obtain analysis results that last for days with CFD or FSI analyses in a very short time. With more detailed and more data sets, deep learning models can be developed and predictions can be made in a very short time. Some studies also draw attention to the advantages of deep learning studies

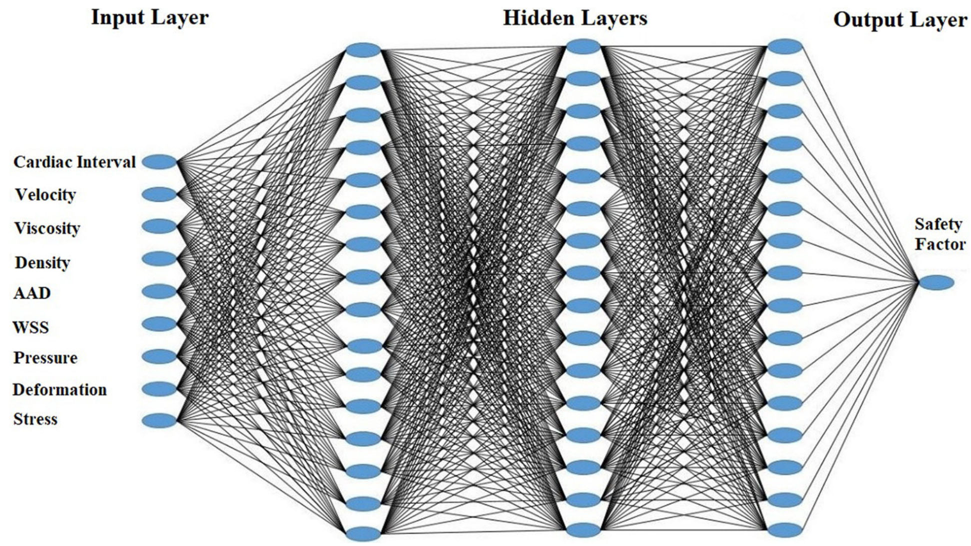


**Fig. 11** ANN Algorithm used in this study

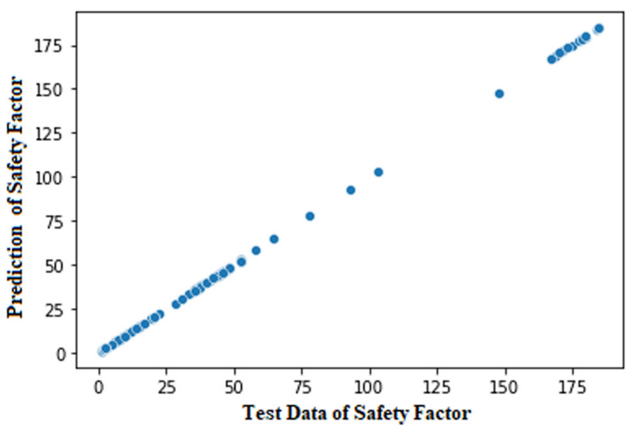


**Fig. 12** Variation of safety factor according to test and prediction data

on vascular flow in terms of computational costs and time. A study performed on von Mises stress on arteries indicates that the ANN algorithm can estimate the stress on arteries with a maximum 9.86% error [55]. A study indicates that CFD simulations are highly expensive in terms of computational cost and time and the ANN algorithm can predict the stress on arteries with an average error of 2.5% [56]. In this study, the rupture risk of the thoracic ascending aortic aneurysm was predicted with 98.6% accuracy by coupling computational fluid dynamics and structural mechanics.

## 5 Conclusion

This study provides a new perspective on thoracic aortic aneurysms in terms of deformation and rupture risk. Patient-specific boundary conditions were applied in numerical analyses for the tomographies of a normal subject and a patient with an aortic aneurysm. Two-way fluid–structure interaction analyses were performed and compared with CFD results. In this way, rigid and elastic artery assumptions were compared to assess effectiveness.

This study aims to provide information for clinical techniques and provide a better estimate of the probability of a rupture. The results show that although FSI analysis has huge computational costs, the FSI analysis should be considered when assessing the risk of rupture. While one of three FSI simulations lasted about 120 h, one of three CFD simulations lasted only 30 h except for segmentation and mesh studies. Evaluating only WSS by rigid artery assumption may not be reasonable to assess rupture risk.

FSI simulations revealed that 2.75 mm, 6.82 mm, and 8.48 mm total deformations were observed in the cases of—19.81 mm, 42.94 mm, and 48.01 mm AAD, respectively. The expansion in AAD caused more deformations than the rate of increase (13.8%, 15.8%, and 17.6%) in the AAD. On the other hand, safety factor results showed that, while it is almost 15 for the normal subject, it is approximately 5 and 2 for the cases of 42.94 mm and 48.01 mm AAD, respectively, under the same boundary conditions. According to these results, the 48.01 mm AAD is seven times more at rupture risk than the normal subject, and the AAD of 42.94 mm is three times more at rupture risk than the normal subject.

Despite all these findings, the most important limitation in FSI analyses is the mechanical properties of arteries. It is hard to obtain the mechanical properties of individuals in terms of both ethical requirements and measurement techniques. Therefore, it is not possible to claim that the results are the same as the actual values in patient-specific vascular flows performed in this study. However, the study aims to assist and shed light on the clinical techniques and aims to show the necessities of FSI despite the increasing computational cost at least three or four times. On the other hand, we claim that FSI analyses are needed to observe the rupture risk of the arteries with huge computational costs and time. However, deep learning studies could be used the reduce computational cost and time by larger datasets. This study presents preliminary work on the deep learning side by the three aortic geometries and 648 data during the cardiac cycle. It could be expanded by hundreds of aortic geometries with huge computational costs and time to shed light on the literature. We conclude that the rupture risk evaluated by the safety factors of the arteries can guide the clinical assessments and predictions performed with FSI and deep learning.

**Acknowledgements** This paper was not financially supported by any foundation.

**Funding** Open access funding provided by the Scientific and Technological Research Council of Türkiye (TÜBİTAK). The authors thank Materialise for providing a trial software version of the Mimics used in the segmentation process.

## Declarations

**Conflict of interest** No potential conflict of interest in this study.

**Ethical Approval** In this study, all measurement techniques have been approved by the Ethics Committee of Alanya Alaaddin Keykubat University, Turkey (10354421-2020/16-17).



## References

1. Jayendiran, R.; Condemi, F.; Campisi, S.; Viallon, M.; Croisille, P.; Avril, S.: Computational prediction of hemodynamical and biomechanical alterations induced by aneurysm dilatation in patient-specific ascending thoracic aortas. Int. J. Numer. Method. Biomed. Eng. **36**, 1–24 (2020). https://doi.org/10.1002/cnm.3326
2. Yeh, H.H.; Rabkin, S.W.; Grecov, D.: Hemodynamic assessments of the ascending thoracic aortic aneurysm using fluid-structure interaction approach. Med. Biol. Eng. Comput. **56**, 435–451 (2018). https://doi.org/10.1007/s11517-017-1693-z
3. Lorenzini, G.; Casalena, E.: CFD analysis of pulsatile blood flow in an atherosclerotic human artery with eccentric plaques. J. Biomech. **41**, 1862–1870 (2008). https://doi.org/10.1016/j.jbiomech.2008.04.009
4. Benim, A.C.; Nahavandi, A.; Assmann, A.: CFD analysis of blood flow in human aorta with experimental validation. In: 7th International Conference on Computational Heat and Mass Transfer (2011)
5. Numata, S.; Itatani, K.; Kanda, K.; Doi, K.; Yamazaki, S.; Morimoto, K.; Manabe, K.; Ikemoto, K.; Yaku, H.: Blood flow analysis of the aortic arch using computational fluid dynamics. Eur. J. Cardio-thoracic Surg. **49**, 1578–1585 (2016). https://doi.org/10.1093/ejcts/ezv459
6. Morris, L.; Delassus, P.; Callanan, A.; Walsh, M.; Wallis, F.; Grace, P.; McGloughlin, T.: 3-D numerical simulation of blood flow through models of the human aorta. J. Biomech. Eng. **127**, 767–775 (2005). https://doi.org/10.1115/1.1992521
7. Brown, A.G.; Shi, Y.; Marzo, A.; Staicu, C.; Valverde, I.; Beerbaum, P.; Lawford, P.V.; Hose, D.R.: Accuracy vs. computational time: translating aortic simulations to the clinic. J. Biomech. **45**, 516–523 (2012). https://doi.org/10.1016/j.jbiomech.2011.11.041
8. Suito, H.; Takizawa, K.; Huynh, V.Q.H.; Sze, D.; Ueda, T.: FSI analysis of the blood flow and geometrical characteristics in the thoracic aorta. Comput. Mech. **54**, 1035–1045 (2014). https://doi.org/10.1007/s00466-014-1017-1
9. Gao, F.; Watanabe, M.; Matsuzawa, T.: Stress analysis in a layered aortic arch model under pulsatile blood flow. Biomed. Eng. Online **5**, 1–11 (2006). https://doi.org/10.1186/1475-925X-5-25
10. Crosetto, P.; Reymond, P.; Deparis, S.; Kontaxakis, D.; Stergiopulos, N.; Quarteroni, A.: Fluid-structure interaction simulation of aortic blood flow. Comput. Fluids **43**, 46–57 (2011). https://doi.org/10.1016/j.compfluid.2010.11.032
11. Campobasso, R.; Condemi, F.; Viallon, M.; Croisille, P.; Campisi, S.; Avril, S.: Evaluation of peak wall stress in an ascending thoracic aortic aneurysm using FSI simulations: effects of aortic stiffness and peripheral resistance. Cardiovasc. Eng. Technol. **9**, 707–722 (2018). https://doi.org/10.1007/s13239-018-00385-z
12. Aksoy, B.; Koru, M.: Estimation of Casting mold interfacial heat transfer coefficient in pressure die casting process by artificial intelligence methods. Arab. J. Sci. Eng. **45**, 8969–8980 (2020). https://doi.org/10.1007/s13369-020-04648-7
13. Gamal, H.; Elkatatny, S.: Prediction model based on an artificial neural network for rock porosity. Arab. J. Sci. Eng. (2021). https://doi.org/10.1007/s13369-021-05912-0
14. Elkatatny, S.: A self-adaptive artificial neural network technique to predict total organic carbon (TOC) based on well logs. Arab. J. Sci. Eng. **44**, 6127–6137 (2019). https://doi.org/10.1007/s13369-018-3672-6
15. Jordanski, M.; Radovic, M.; Milosevic, Z.; Filipovic, N.; Obradovic, Z.: Machine learning approach for predicting wall shear distribution for abdominal aortic aneurysm and carotid bifurcation models. IEEE J. Biomed. Heal. Informat. **22**, 537–544 (2018). https://doi.org/10.1109/JBHI.2016.2639818
16. Liang, L.; Liu, M.; Martin, C.; Sun, W.: A deep learning approach to estimate stress distribution: a fast and accurate surrogate of finite-element analysis. J. R. Soc. Interface **15**, 20170844 (2018). https://doi.org/10.1098/rsif.2017.0844
17. Etli, M.; Canbolat, G.; Karahan, O.; Koru, M.: Numerical investigation of patient-specific thoracic aortic aneurysms and comparison with normal subject via computational fluid dynamics (CFD). Med. Biol. Eng. Comput. **59**, 71–84 (2021). https://doi.org/10.1007/s11517-020-02287-6
18. Savabi, R.; Nabaei, M.; Farajollahi, S.; Fatouraee, N.: Fluid structure interaction modeling of aortic arch and carotid bifurcation as the location of baroreceptors. Int. J. Mech. Sci. **165**, 105222 (2020). https://doi.org/10.1016/j.ijmecsci.2019.105222
19. Kleinstreuer, C.; Li, Z.; Farber, M.A.: Fluid-structure interaction analyses of stented abdominal aortic aneurysms. Annu. Rev. Biomed. Eng. **9**, 169–204 (2007). https://doi.org/10.1146/annurev.bioeng.9.060906.151853
20. Gao, F.; Guo, Z.; Sakamoto, M.; Matsuzawa, T.: Fluid-structure interaction within a layered aortic arch model. J. Biol. Phys. **32**, 435–454 (2006). https://doi.org/10.1007/s10867-006-9027-7

21. Febina, J.; Sikkandar, M.Y.; Sudharsan, N.M.: Wall shear stress estimation of thoracic aortic aneurysm using computational fluid dynamics. Comput. Math. Methods Med. (2018). https://doi.org/10.1155/2018/7126532
22. Fanni, B.M.; Sauvage, E.; Celi, S.; Norman, W.; Vignali, E.; Landini, L.; Schievano, S.; Positano, V.; Capelli, C.: A proof of concept of a non-invasive image-based material characterization method for enhanced patient-specific computational modeling. Cardiovasc. Eng. Technol. **11**, 532–543 (2020). https://doi.org/10.1007/s13239-020-00479-7
23. García-Herrera, C.M.; Atienza, J.M.; Rojo, F.J.; Claes, E.; Guinea, G.V.; Celentano, D.J.; García-Montero, C.; Burgos, R.L.: Mechanical behaviour and rupture of normal and pathological human ascending aortic wall. Med. Biol. Eng. Comput. **50**, 559–566 (2012). https://doi.org/10.1007/s11517-012-0876-x
24. Lei, Y.; Chen, M.; Xiong, G.; Chen, J.: Influence of virtual intervention and blood rheology on mass transfer through thoracic aortic aneurysm. J. Biomech. **48**, 3312–3322 (2015). https://doi.org/10.1016/j.jbiomech.2015.06.022
25. Keramati, H.; Birgersson, E.; Ho, J.P.; Kim, S.; Chua, K.J.; Leo, H.L.: The effect of the entry and re-entry size in the aortic dissection: a two-way fluid–structure interaction simulation. Biomech. Model. Mechanobiol. **19**, 2643–2656 (2020). https://doi.org/10.1007/s10237-020-01361-0
26. Bonfanti, M.; Balabani, S.; Alimohammadi, M.; Agu, O.; Homer-Vanniasinkam, S.; Díaz-Zuccarini, V.: A simplified method to account for wall motion in patient-specific blood flow simulations of aortic dissection: Comparison with fluid-structure interaction. Med. Eng. Phys. **58**, 72–79 (2018). https://doi.org/10.1016/j.medengphy.2018.04.014
27. Mendez, V.; Di Giuseppe, M.; Pasta, S.: Comparison of hemodynamic and structural indices of ascending thoracic aortic aneurysm as predicted by 2-way FSI, CFD rigid wall simulation and patient-specific displacement-based FEA. Comput. Biol. Med. **100**, 221–229 (2018). https://doi.org/10.1016/j.compbiomed.2018.07.013
28. Khanafer, K.M.; Bull, J.L.; Berguer, R.: Fluid-structure interaction of turbulent pulsatile flow within a flexible wall axisymmetric aortic aneurysm model. Eur. J. Mech. B/Fluids. **28**, 88–102 (2009). https://doi.org/10.1016/j.euromechflu.2007.12.003
29. Sharzehee, M.; Khalafvand, S.S.; Han, H.C.: Fluid-structure interaction modeling of aneurysmal arteries under steady-state and pulsatile blood flow: a stability analysis. Comput. Methods Biomech. Biomed. Engin. **21**, 219–231 (2018). https://doi.org/10.1080/10255842.2018.1439478
30. Rissland, P.; Alemu, Y.; Einav, S.; Ricotta, J.; Bluestein, D.: Abdominal aortic aneurysm risk of rupture: patient-specific FSI simulations using anisotropic model. J. Biomech. Eng. **131**, 031001 (2009). https://doi.org/10.1115/1.3005200
31. Leung, J.H.; Wright, A.R.; Cheshire, N.; Crane, J.; Thom, S.A.; Hughes, A.D.; Xu, Y.: Fluid structure interaction of patient specific abdominal aortic aneurisms: a comparison with solid stress models. Biomed. Eng. Online **5**, 1–15 (2006). https://doi.org/10.1186/1475-925X-5-33
32. Cho, Y.I.; Kensey, K.R.: Effects of the non-Newtonian viscosity of blood on flows in a diseased arterial vessel. Part 1: steady flows. Biorheology **28**, 241–262 (1991). https://doi.org/10.3233/BIR-1991-283-415
33. Canbolat, G.; Eetli, M.; Karahan, O.; Koru, M.; Korkmaz, E.: Investigation of vascular flow in a thoracic aaorta in terms of flow models and blood rheology via computational fluid dynamics (CFD). J. Mech. Med. Biol. (2023). https://doi.org/10.1142/S021951942350094X
34. Lee, C.J.; Zhang, Y.; Takao, H.; Murayama, Y.; Qian, Y.: A fluid-structure interaction study using patient-specific ruptured and unruptured aneurysm: the effect of aneurysm morphology, hypertension and elasticity. J. Biomech. **46**, 2402–2410 (2013). https://doi.org/10.1016/j.jbiomech.2013.07.016
35. Darıcık, F.; Canbolat, G.; Koru, M.: Investigation of a fiber reinforced polymer composite tube by two way coupling fluid- structure interaction. Coupled Syst. Mech. **11**, 315–333 (2022). https://doi.org/10.12989/csm.2022.11.4.315
36. LeCun, Y.; Bengio, Y.; Hinton, G.: Deep learning. Nature **521**, 436–444 (2015). https://doi.org/10.1038/nature14539
37. Gardner, M.W.; Dorling, S.R.: Artificial neural networks (the multilayer perceptron) - a review of applications in the atmospheric sciences. Atmos. Environ. **32**, 2627–2636 (1998). https://doi.org/10.1016/S1352-2310(97)00447-0
38. Kaneko, H.: Beware of r 2 even for test datasets: using the latest measured y-values (r 2 LM) in time series data analysis. J. Chemom. **33**, e3093 (2019). https://doi.org/10.1002/cem.3093
39. Blacher, J.; Safar, M.E.: Large-artery stiffness, hypertension and cardiovascular risk in older patients. Nat. Clin. Pract. Cardiovasc. Med. **2**, 450–455 (2005). https://doi.org/10.1038/ncpcardio0307
40. Flint, A.C.; Conell, C.; Ren, X.; Banki, N.M.; Chan, S.L.; Rao, V.A.; Melles, R.B.; Bhatt, D.L.: Effect of systolic and diastolic blood pressure on cardiovascular outcomes. N. Engl. J. Med. **381**, 243–251 (2019). https://doi.org/10.1056/NEJMoa1803180
41. Vorp, D.A.; Schiro, B.J.; Ehrlich, M.P.; Juvonen, T.S.; Ergin, M.A.; Griffith, B.P.: Effect of aneurysm on the tensile strength and biomechanical behavior of the ascending thoracic aorta. Ann. Thorac. Surg. **75**, 1210–1214 (2003). https://doi.org/10.1016/S0003-4975(02)04711-2
42. Chung, A.W.Y.; Au Yeung, K.; Sandor, G.G.S.; Judge, D.P.; Dietz, H.C.; van Breemen, C.: Loss of elastic fiber integrity and reduction of vascular smooth muscle contraction resulting from the upregulated activities of matrix metalloproteinase-2 and -9 in the thoracic aortic aneurysm in Marfan syndrome. Circ. Res. **101**, 512–522 (2007). https://doi.org/10.1161/CIRCRESAHA.107.157776
43. Gao, F.; Ohta, O.; Matsuzawa, T.: Fluid-structure interaction in layered aortic arch aneurysm model: assessing the combined influence of arch aneurysm and wall stiffness. Australas. Phys. Eng. Sci. Med. **31**, 32–41 (2008). https://doi.org/10.1007/BF03178451
44. Alimohammadi, M.; Sherwood, J.M.; Karimpour, M.; Agu, O.; Balabani, S.; Díaz-Zuccarini, V.: Aortic dissection simulation models for clinical support: fluid-structure interaction vs. rigid wall models. Biomed. Eng. Online **14**, 1–16 (2015). https://doi.org/10.1186/s12938-015-0032-6
45. Janela, J.; Moura, A.; Sequeira, A.: Absorbing boundary conditions for a 3D non-Newtonian fluid-structure interaction model for blood flow in arteries. Int. J. Eng. Sci. **48**, 1332–1349 (2010). https://doi.org/10.1016/j.ijengsci.2010.08.004
46. Castro, M.A.; Olivares, M.C.A.; Putman, C.M.; Cebral, J.R.: Unsteady wall shear stress analysis from image-based computational fluid dynamic aneurysm models under Newtonian and Casson rheological models. Med. Biol. Eng. Comput. **52**, 827–839 (2014). https://doi.org/10.1007/s11517-014-1189-z
47. Palmer, R.F.; Wheat, M.W.: Treatment of dissecting aneurysms of the aorta. Ann. Thorac. Surg. **4**, 38–52 (1967). https://doi.org/10.1016/S0003-4975(10)66476-4
48. Shojima, M.: Magnitude and role of wall shear stress on cerebral aneurysm. Computational fluid dynamic study of 20 middle cerebral artery aneurysms. Stroke **35**, 2500–2505 (2004)
49. Munarriz, P.M.; Gómez, P.A.; Paredes, I.; Castaño-Leon, A.M.; Cepeda, S.; Lagares, A.: Basic principles of hemodynamics and cerebral aneurysms. World Neurosurg. **88**, 311–319 (2016). https://doi.org/10.1016/j.wneu.2016.01.031
50. Lantz, J.; Renner, J.; Karlsson, M.: Wall shear stress in a subject specific human aorta - influence of fluid-structure interaction. Int. J. Appl. Mech. **3**, 759–778 (2011). https://doi.org/10.1142/S1758825111001226

51. Reymond, P.; Crosetto, P.; Deparis, S.; Quarteroni, A.; Stergiopulos, N.: Physiological simulation of blood flow in the aorta: comparison of hemodynamic indices as predicted by 3-D FSI, 3-D rigid wall and 1-D models. Med. Eng. Phys. **35**, 784–791 (2013). https://doi.org/10.1016/j.medengphy.2012.08.009
52. Tan, F.P.P.; Torii, R.; Borghi, A.; Mohiaddin, R.H.; Wood, N.B.; Xu, X.Y.: Fluid-structure interaction analyses of wall stress and flow patterns in a thoracic aortic aneurysm. Int. J. Appl. Mech. **01**, 179–199 (2009). https://doi.org/10.1142/S1758825109000095
53. Lasheras, J.C.: The biomechanics of arterial aneurysms. Annu. Rev. Fluid Mech. **39**, 293–319 (2007). https://doi.org/10.1146/annurev.fluid.39.050905.110128
54. Juvela, S.: Prehemorrhage risk factors for fatal intracranial aneurysm rupture. Stroke **34**, 1852–1857 (2003). https://doi.org/10.1161/01.STR.0000080380.56799.DD
55. Madani, A.; Bakhaty, A.; Kim, J.; Mubarak, Y.; Mofrad, M.R.K.: Bridging finite element and machine learning modeling: stress prediction of arterial walls in atherosclerosis. J. Biomech. Eng. **141**, 084502 (2019). https://doi.org/10.1115/1.4043290
56. Su, B.; Zhang, J.M.; Zou, H.; Ghista, D.; Le, T.T.; Chin, C.: Generating wall shear stress for coronary artery in real-time using neural networks: feasibility and initial results based on idealized models. Comput. Biol. Med. **126**, 104038 (2020). https://doi.org/10.1016/j.compbiomed.2020.104038